Ultrasonics 94 (2019) 50–59

Contents lists available at ScienceDirect

Ultrasonics

journal homepage: www.elsevier.com/locate/ultras

Experimental analysis of surface detection methods for two-medium imaging with a linear ultrasonic array

M.Y. Matuda*, F. Buiochi*, J.C. Adamowski

Mechatronics Engineering Department, School of Engineering at the University of Sao Paulo, Sao Paulo, Brazil

ARTICLE INFO

Keywords:
Ultrasound imaging
Surface detection
Ultrasonic array transducer

ABSTRACT

In ultrasonic nondestructive testing, when using an ultrasonic linear array transducer for imaging objects with nonplanar surfaces, a coupling medium must be used. To compensate for the refraction at the coupler-object interface, its shape must be known. Two methods for surface detection of convex objects in immersion are proposed, using the same linear array transducer for surface detection and for SAFT imaging. One is based on imaging technique and the other is based on the time-of-flight of the echoes on the captured ultrasonic signals. The accuracy and performance of the two methods are compared experimentally with an existing fast method called pitch-catch. The proposed methods produced smaller errors in part of the tested configurations, with a slower performance compared with the pitch-catch method. After the surface detection, in the SAFT image formation phase, the delays are calculated through a simple and fast proposed technique to determine the fastest paths, following the Fermat's principle. Images are formed for nine distinct array element groups, and then combined using the effective aperture technique. The results show that the developed methods allow interactive two-medium image formation on a general-purpose CPU.

1. Introduction

In ultrasonic array imaging for nondestructive testing, when the position of the transducer relative to the object changes during the testing, or the transducer needs to analyze parts of the object with different surface shapes, solid adapters are not adequate, because they would need to be frequently replaced. A good solution is the utilization of flexible transducers, which are capable of real-time imaging [1] when combined with sensors to indicate the element positions. Their problem is the higher complexity compared with conventional arrays.

Another option is the use of a flexible solid or fluid coupling material. But when the propagation speed in the coupling material is very different from the speed in the object, the refraction at the interface must be taken into account. The refraction compensation requires the detection of the shape and position of the interface. Detecting the interface using the ultrasound array itself reduces the hardware complexity, because the need for additional position sensors is avoided. On the other hand, the processing complexity is higher due to the calculations for refraction compensation, and a temperature sensor may be needed if the propagation speed in the coupling medium is highly dependent on the temperature.

Detection of surfaces may be executed by first obtaining an image, and then utilizing a segmentation algorithm [2]. When the surface is convex or planar, the segmentation algorithm may be replaced by a simple peak detection [3], but in this case an image is needed for each peak point, therefore a high processing power is still needed. Methods that use image formation techniques are referred to as imaging-based in this text. Since imaging-based methods use summations of signals, they have some capability to ignore distorted echoes that occur due to transducer element directivity.

There are methods that use the time-of-flight of the echoes contained in the captured signals [4–7], for generic surfaces. Because they avoid the image formation process, they tend to be fast in processing. These methods are referred to as time-of-flight-based in this text. A recent solution is the SAUL (Surface Adaptive Ultrasound) method [6], in which the times-of-flight of the first echoes in the captured signals are utilized to iteratively make the wavefront parallel to the interface at incidence, which eliminates the refraction problem. Its disadvantages are that it is currently not focused, and it needs an acquisition equipment with an active channel for each array element, which is more expensive than multiplexed systems.

In this work, two methods of interface detection are proposed, for convex or planar surfaces. One is imaging-based, the arc method, which does not need to form complete images, and consequently may be faster than other imaging-based methods. The other is time-of-flight-based, the tangent curve method. Both methods can use multiplexed

* Corresponding authors.
E-mail addresses: marcelo@mym.eng.br (M.Y. Matuda), fbuiochi@usp.br (F. Buiochi).

https://doi.org/10.1016/j.ultras.2018.12.004
Received 16 August 2018; Received in revised form 9 November 2018; Accepted 5 December 2018
Available online 07 December 2018
0041-624X/

acquisition systems. One objective is to verify if imaging-based methods can be as fast as time-of-flight-based methods, and if there is any advantage to the former. To this end, the accuracy and processing speed of the proposed methods are compared with an existing method called pitch-catch [7]. The pitch-catch method was selected because it is a high-quality, fast and easy to implement method. Image formation with automatic refraction compensation, or auto-focusing [7], can be executed in real-time using GPUs [8], provided a fast communication between the acquisition system and the computer is available. This work verifies if current general-purpose CPUs are able to execute the same processing interactively. The result of the interface detection is then utilized in image formation by synthetic aperture technique, with automatic refraction compensation, in water immersion.

2. Theory

The inspection of objects in immersion with automatic refraction compensation may be divided in three steps: the surface detection, the curve fitting and the image formation. In the first step, points are obtained near the real surface geometry. These points are then used in a curve fitting in the second step. The fitted curve is utilized in the third step to obtain the minimum time-of-flight trajectories according to the Fermat's principle. The delays are calculated from the trajectories, and the image can finally be formed. To reduce the data size and the processing time, the same data is utilized in the first and third steps, and only one element transmits in each active element group in the multiplexed array.

2.1. The arc method of surface detection

The arc method is an imaging-based method, but it does not need the formation of entire images. First a central element e_c in the active element group transmits and all the active receive elements in the group capture signals. Using the signal received by the central element, the time-of-flight Δt_c is measured. With the propagation speed c_1 in water the distance $r_t = c_1 \Delta t_c/2$ from the central element to the surface is obtained. A circular arc is then defined, centered on the central element and with radius r_t (Fig. 1). In the figure, the object is cylindrical, but any convex or planar surface can be used.

To determine the angle α for the point P of tangency in Fig. 1, the formula for synthetic aperture imaging is applied over the obtained circular arc. In synthetic aperture imaging, the value at the image point with index g for the base element e_b, which is the first element of the active group in the multiplexed array, is given by:

$$S_{e_{bg}} = \sum_{j=e_{r1}}^{e_{r2}} a_j s_{ij}\left(\Delta t_{igj}\right) \tag{1}$$

where $i = e_c$, e_{r1} and e_{r2} are the first and last active receive elements respectively, a_j is the receive apodization coefficient, s_{ij} is the captured signal for transmit element i and receive element j, and Δt_{igj} is the calculated time-of-flight for the fastest path starting from the transmit element i, passing through the grid point with index g and ending at the receive element j, according to the Fermat's principle. In the surface detection step only one medium is considered, therefore the fastest path is represented by a straight line from the transmit element to the point with index g, and another straight line to the receive element.

The following steps are then executed:

- Define a threshold to detect the central lobe in the curve of $S_{e_{bg}}$ over the arc. In this work the threshold is equal to half the peak value.
- Obtain the index i_1 of the first curve point with value above the threshold, searching from the first to the last index of the curve over the arc.
- Obtain the index i_2 of the first curve point with value above the threshold, searching from the last to the first index of the curve over the arc.
- Obtain the index m, the nearest integer to the value of $(i_1 + i_2)/2$. The index m is approximately the center of the main lobe.
- The angle α for point P (Fig. 1) is finally obtained by the position of the point with index m over the circular arc. The hypothesis is that the center of the main lobe is approximately the point P of tangency.

An odd number of active receive elements is utilized, with equal number of elements to the left and to the right of the central element. Because the radius r_t is obtained from the time-of-flight and the angle α from an image formation formula, the method may be considered hybrid. Since the calculation is executed over a curve instead of over a grid, the processing may be faster than other imaging-based methods.

In practice the arc must be discretized. The effect of the discretization was simulated using a cylindrical object with radius R_{cyl} whose center is on the z-axis, and a transmit element at the origin (Fig. 2). If the maximum value over the arc is at the point P but, due to discretization, the point (x_{arc}, z_{arc}) was selected, the detected point is not over the surface, but at a distance to the surface given by:

$$\varepsilon_{arc} = \sqrt{x_{arc}^2 + ((r_t + R_{cyl}) - z_{arc})^2} - R_{cyl} \tag{2}$$

where $x_{arc} = r_t \sin(\gamma)$ and $z_{arc} = r_t \cos(\gamma)$.

In Fig. 3, the error ε_{arc} is plotted, for $R_{cyl} = 15$ mm and $r_t = 15$ mm. For an arc offset (Fig. 2) of 0.3 mm, the error is only 6 µm, and this shows that the arc discretization does not need to be very fine, which contributed to faster processing.

2.2. The tangent curve method of surface detection

The tangent curve method is a time-of-flight-based method, because its calculations need only the time-of-flight of the surface echoes. Given a combination of transmit and receive elements, the echo time-of-flight is converted to distance using the propagation speed, and this travel distance provides range information, but do not yet define a direction. The space of possible reflector positions is an ellipse with one focus on the transmit element and the other on the receive element. With more combinations of transmit and receive elements, other ellipses are defined. The interface is then the curve tangent to all those ellipses. If the surface were not tangent to the ellipses, it would generate echoes

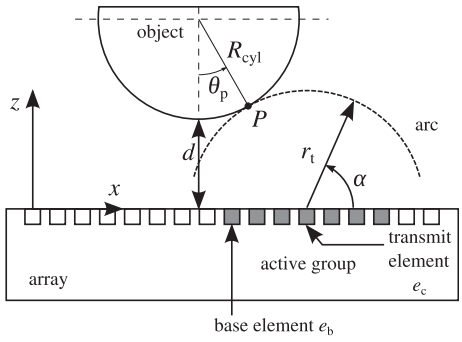

Fig. 1. The arc method.

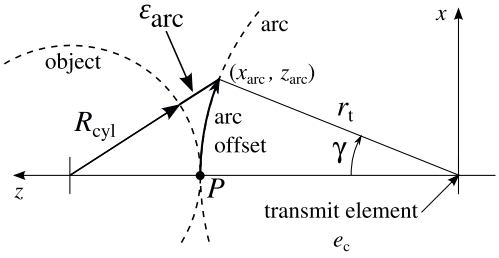

Fig. 2. Arc discretization error ε_{arc}.

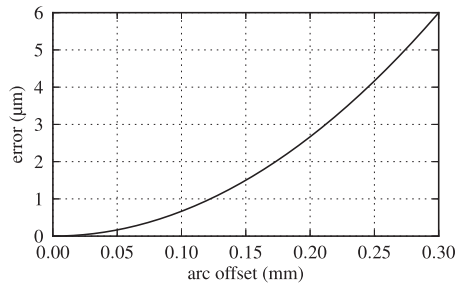

Fig. 3. Error ε_{arc} due to an arc offset relative to the point of tangency.

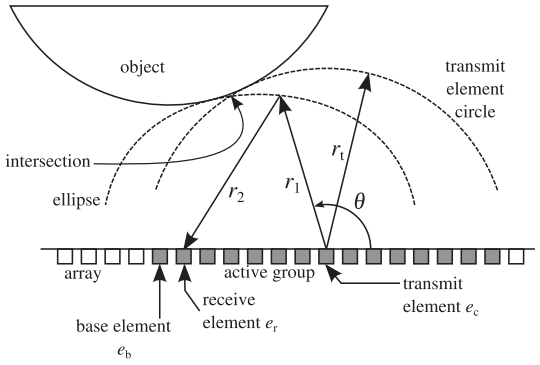

Fig. 4. The tangent curve method.

arriving earlier or later than the already detected echoes, which would be a contradiction. This approach has been utilized in other works [4,9]. The contribution of the tangent curve method is the delimitation of the region of interest.

In this method, the transmit element is always a central element with index e_c (Fig. 4). Furthermore, there is an odd number of receive elements, in the same conditions as the arc method. The receive element index is named e_r. Since the number of receive elements is limited, the number of formed ellipses is also limited, which makes the tangency points restricted to a region over the object surface. Outside this region the object surface is far away from the ellipses, therefore the search for the tangent curve must only be executed in this limited region, the region of interest. To define the limits for the region, first a circular arc centered on the transmit element e_c and an ellipse with foci on the transmit and receive elements are considered (Fig. 4). Both curves are tangent to the object surface. The arc radius is given by $r_t = c_1\Delta t_c/2$, where Δt_c is the time-of-flight of the surface echo when the element e_c is transmitting and receiving. For the ellipse, $2a_{el} = c_1\Delta t_r$ where a_{el} is the semimajor axis, and $2c_{el} = |e_c - e_r|d_p$ is the distance between foci. The time Δt_r is the time-of-flight when the element e_c is transmitting and the element e_r is receiving, and d_p is the array pitch. The ellipse eccentricity is calculated by $e_{el} = c_{el}/a_{el}$. Also the distance from the central element to a point on the ellipse is given by [10]:

$$r_1 = \frac{a_{el}(1 - e_{el}^2)}{1 \pm e_{el}\cos\theta} \tag{3}$$

where the plus sign in the denominator is used when the receive element is to the left of the central element, and the minus sign when the receive element is to the right.

In the intersection between the ellipse and the arc, r_1 is equal to r_t, and with (3):

$$\cos\theta_i = \pm\left(\frac{a_{el}(1 - e_{el}^2) - r_t}{r_t e_{el}}\right) \tag{4}$$

where the sign at the left of the fraction is chosen like in (3), and θ_i is the angle at the intersection between the circular arc and an ellipse.

If the experiment were noiseless, the highest value of the angle θ_i,

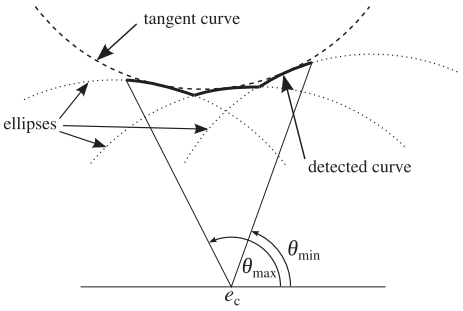

Fig. 5. Difference between the tangent curve and the detected curve in the tangent curve method.

considering all the ellipses defined by the corresponding receive elements, would be obtained for the leftmost receive element, and the lowest value would be obtained for the rightmost receive element. But in real conditions this may not occur. For this reason, the angle θ_i was obtained for all the intersections, and the lowest and the highest angles, θ_{min} and θ_{max} respectively, were considered the limits for the region in which the tangent curve is determined (Fig. 5). In this region, the angle θ is discretized, and for each intermediate angle θ, the maximum value of r_1 is chosen, considering all the ellipses. The value of r_1 is calculated by (3). With θ and the maximum r_1 the position of a surface point is defined. There is one point for each intermediate value of θ. In this way, the tangent curve method generates many points for each element group, in contrast to the arc method, which generates only one point per group.

Since the array pitch is not infinitely small, the obtained curve is not smooth, and is only approximately the tangent curve. This may be visualized in Fig. 5, where the errors are exaggerated.

3. Material and methods

The analyzed object is a cylindrical aluminum block with a height of 40 mm, and through holes with a diameter of 3 mm simulating defects (Figs. 6 and 7). The longitudinal propagation speed c_2 in the block was measured by pulse-echo and was considered constant for all the experiments. The center of the block was positioned at the central axis of the array, allowing a symmetric experiment. Four values for the distance d in Fig. 1 were utilized, 15, 20, 30 and 40 mm. One purpose of the cylindrical object is to show how the surface detection methods work for varying values of the angle θ_p (Fig. 1).

The coupling medium is water, which has low losses. To obtain an accurate propagation speed in water, the water temperature was measured by a digital thermometer model HD 2127.2 (Delta OHM, Italy), with a TP 472 I (Pt100) probe. The propagation speed c_1 in water was calculated using a formula proposed by Marczak [11]. The temperature measurement was done before each set of signal acquisitions.

The signals were acquired by a Sitau MX 32:128 (Dasel Sistemas, Spain), with sampling frequency f_s = 40 MHz and 12-bit samples. The equipment has 32 channels, multiplexed to 128. The utilized linear array, from Imasonic (France), has central frequency f_c = 5 MHz, 128 elements, pitch of 0.6 mm and elements with a width of 0.5 mm. The

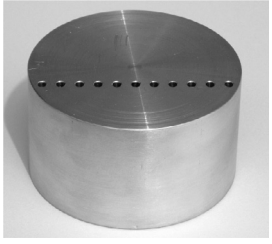

Fig. 6. The aluminum block utilized in the experiments.

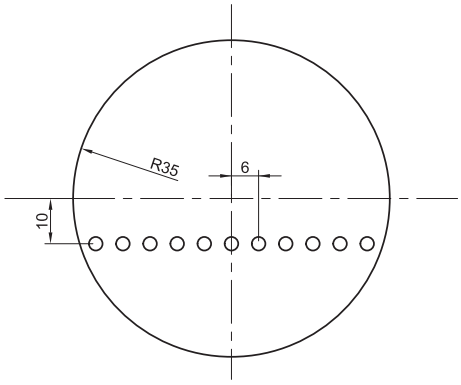

Fig. 7. Dimensions in mm of the aluminum block utilized in the experiments.

array elements are numbered from 0 to 127 in this work. For all the experiments, the chosen central element had index 15, relative to the base element. All the analyzed methods use the same acquired data.

For the processing, a custom multithreaded C++ software was executed on a PC with an Intel Core i7 4790 processor. The software was not well optimized, as more SIMD (Single Instruction, Multiple Data) instructions could have been used. However, needless recalculations have been avoided by storing values that were used more than once. The GNU compiler (GCC) and libraries were utilized, on an operating system using the Linux kernel for the x86-64 architecture.

3.1. Acquisition system calibration

Since real acquisition systems and transducers do not have ideal responses, they must be calibrated if high accuracy is needed. For 48 of the 128 array elements, the following procedure was executed: using a planar reflector, parallel to the frontal face of the transducer at a distance $d = 40$ mm, the average of 64 acquisitions was calculated, and then interpolated with output rate $\bar{f}_s = 16 f_s$. In each resulting signal, a segment was selected. The start of the segment is the instant $t_d = (2d)/c_1 = (2{\cdot}40\text{ mm})/c_1$, the moment at which a Dirac delta would be received if the system had an ideal response. The end of the segment was selected arbitrarily, at an instant after the echo has been faded out. The selected signal segments from the 48 elements were then averaged, resulting in the reference signal s_{ref}, which was downsampled back to $f_s = 40$ MHz (Fig. 8). The constant c_1 is the propagation speed in water, obtained from the measured temperature. The choice of number of array elements for calibration is arbitrary, but it must be high enough to smooth out the differences between the responses of the elements.

The cross-correlation of the reference signal s_{ref} and a captured signal results in a signal whose peak is at the time-of-flight Δt. From c_1 and the time-of-flight Δt the travel distance can be obtained by $d_t = c_1 \Delta t$.

Other methods of time-of-flight detection could also be utilized, such as peak of the envelope or threshold detection. The cross-correlation method is in theory less sensitive to noise than the threshold detection method, because the former works as a band-pass filter, when using the reference signal s_{ref}.

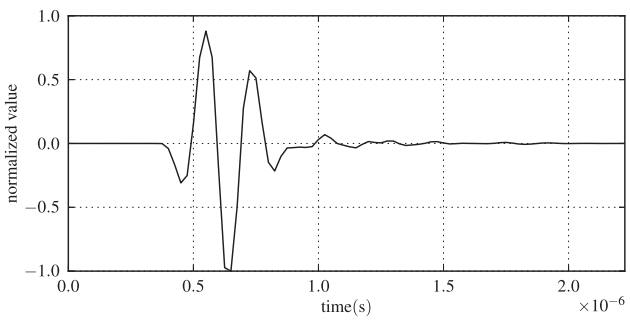

Fig. 8. The reference signal s_{ref}.

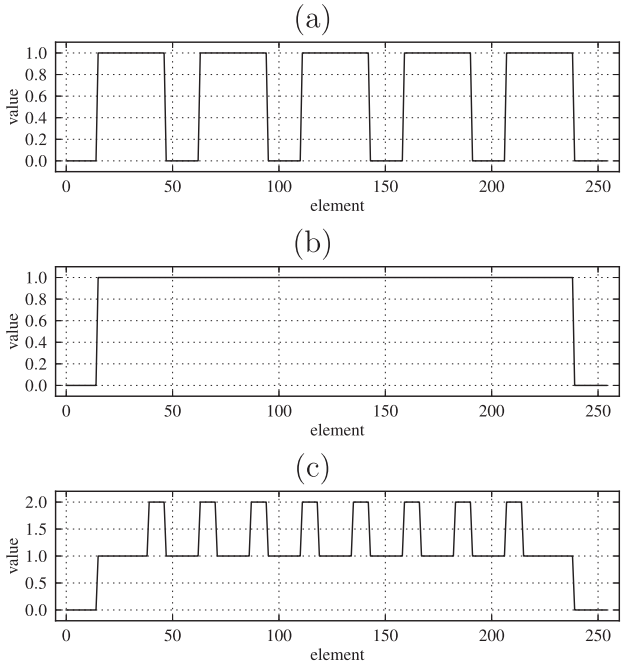

Fig. 9. Effective aperture for the combined image, without apodization, for (a) 5 groups, (b) 7 groups and (c) 9 groups.

3.2. Number of element groups

The surface detection and the image formation use the same signal data, therefore the choice of the number of element groups must take into account the two procedures, because the acquisition system is multiplexed. The number of groups was chosen using the following conditions: the first element of the first group is the first element of the array, the last element of the last group is the last element of the array, the spacing between groups is uniform and there is a central group at the center of the array. These criteria are guided by uniformity, symmetry and maximum utilization of the array. Four values that follow these conditions are 3, 5, 7 and 9, for groups of 32 elements and an array with 128 elements. In the image formation, partial images formed using only one of the element groups are combined by coherent summation, with the help of the effective aperture technique [12]. Less than seven element groups are not adequate, because in these cases the effective aperture has nulls that cannot be eliminated with apodization (Fig. 9a). For nine groups, the effective aperture has protuberances (Fig. 9c), but they can be eliminated with receive apodization (Fig. 10). This apodization is only used in the image formation, not in the surface detection phase. In the figures, the number of elements is greater than 128 because they show the result of the convolution between the transmit and receive apertures. The greater the number of groups, the more points in the curve fitting, which is good for error attenuation, but also the greater the amount of data and computing power needs. The number of nine groups was chosen, even though with seven groups the apodization is not needed (Fig. 9b). With nine groups, there is some superposition of data, shown by the protuberances in Fig. 9c, and the transitions in the effective aperture with apodization are smoother compared with the case with seven groups.

The use of groups of 32 elements from an array of 128 elements is due to the hardware utilized in the experiments, the same analysis could be done in a different hardware. In Fig. 11 the 9 groups of elements can be visualized. Even though the experiment is symmetric,

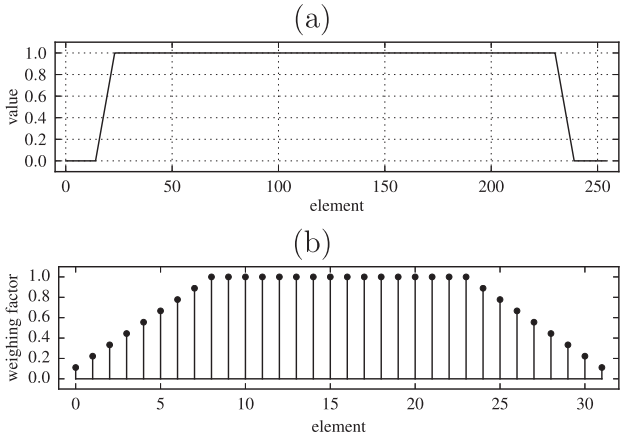

Fig. 10. (a) Effective aperture for the combined image with apodization for 9 groups, and (b) the respective receive apodization function.

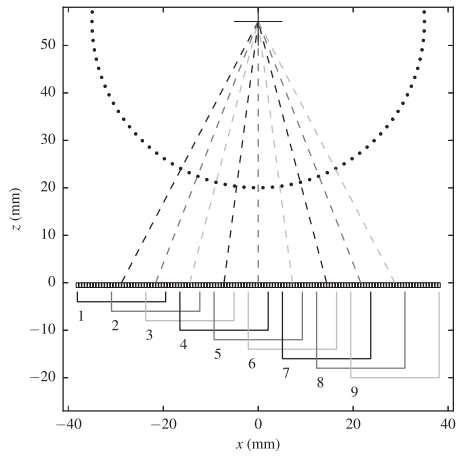

Fig. 11. Image showing the 9 groups of elements. The group ranges are indicated at the bottom of the image. The array elements are at $z = 0$, and the object is indicated by the dotted line. The dashed lines connect the centers of each group to the center of the object.

each group sees the object from a different perspective. Since the surface detection methods use one group at a time, this experimental configuration allows the analysis of the behaviour of each method for different relative positions between the object and each group. Moreover, four values for the distance d in Fig. 1 were utilized, which increased the number of different experimental configurations.

3.3. Preparation of signals

In the arc, tangent curve and pitch-catch methods, the captured ultrasound signals were interpolated and cross-correlated with the reference signal s_{ref}. The time-of-flight was then obtained by the peak of the resulting signal.

In the image formation step, the captured signals were interpolated, high-pass filtered and converted to analytic signals with the help of the Hilbert transform. The image formation then utilized these complex-valued signals. Processing these complex-valued signals is heavier than the original signals, but if the Hilbert transform were executed after the image formation some artifacts would appear due to the discontinuities at the interface. And the utilization of analytic signals in the image formation allowed the use of a coarser image grid.

In the reference signal s_{ref}, the time delay between the start and the peak of the envelope was subtracted from the captured signals in the image formation phase.

The captured signals and s_{ref} were interpolated with output sample rate $\bar{f}_s = 4f_s$ in all experiments. With this sampling rate the maximum absolute distance error in the surface detection, due to the time discretization, is 4.7 μm in water. The low-pass filter employed in the interpolations uses a sinc function multiplied by a Kaiser window, with 80 dB of minimum attenuation in the stopband. After the interpolation, when a signal value was needed for an offset between two discrete signal positions, the value was linearly interpolated. All filterings and cross-correlations were processed in the frequency domain.

3.4. Surface detection

In the surface detection step, the error between the detected points and the reference circle, the circle that is considered the real shape of the object, is given by:

$$\varepsilon_{\text{ref}} = \sqrt{(x_p - x_c)^2 + (z_p - z_c)^2} - R_{\text{cyl}} \tag{5}$$

where (x_p, z_p) are the coordinates of the detected point, (x_c, z_c) are the coordinates of the center of the reference circle and R_{cyl} is its radius. Similarly, the error between the detected points and the fitted circle is given by:

$$\varepsilon_{\text{fit}} = \sqrt{(x_p - \bar{x}_c)^2 + (z_p - \bar{z}_c)^2} - \overline{R}_{\text{cyl}} \tag{6}$$

where $(\bar{x}_c, \bar{z}_c)$ are the coordinates of the center of the fitted circle and $\overline{R}_{\text{cyl}}$ is its radius.

For both arc and tangent curve methods, the arc points were separated by $\lambda_1/4$, where λ_1 is the wavelength in water at f_c.

For the arc method, a simple simulation was defined. For each combination of transmit and receive elements, the fastest path was determined by iterative search, considering paths starting in the transmit element, reflecting on the reference circle and arriving at the receive element. From c_1 and the fastest path, the time-of-flight Δt was obtained. Then in the simulated signal, the reference signal s_{ref} was inserted at the instant Δt. This simulation considers that the signal shape does not depend on the distance d or the angle θ_p (defined in Fig. 1).

3.5. Curve fitting

Since the analyzed object is cylindrical, a circle was fitted to the points obtained in the surface detection step, using the Pratt method [13] as implemented by [14]. Other convex curve shapes can be used, but the curve must be smooth, because the number of detected points is low, specially for the arc method.

3.6. Image formation

After the detection of the interface, the delays must be calculated for the image formation, considering the coupling medium and the object. According to the Fermat's principle, the fastest path must be considered in this calculation. In this process an interface point is selected for each combination of array element and image point. For planar interfaces the problem may be solved analytically [15], but for non-planar interfaces the search must be optimized [16] if a high computing power is not available.

The utilized strategy is to process column by column in a rectangular image grid. The columns are vertical, following the z-axis. Lines are horizontal, following the x-axis. In each column, the processing starts from the interface and continues to the last line at the top of the image. In Figs. 26 and 27 the big circle indicated by dotted lines is the interface, and the topmost line of pixels is the last line. For the first point in each column, the iterative search is done on all the interface, in two discretization levels. For the other grid points in the column, the search is done around the interface point selected for the previous grid point. For the configuration in the experiments, with interface spacing equal to $\lambda_2/4$, where λ_2 is the longitudinal wavelength in aluminum at

f_c, in almost all cases $|n_k - n_{k-1}| \leq 1$, where n_k is the index of the selected interface point in iteration k, with the exception of image grid points near the interface. In other words, the number of distance calculations for each image point is less than a small constant value in most cases, and this is good for performance. This technique does not work for generic surfaces, because with some complex shapes there might be a large gap between the current and previous selected points.

The image is obtained by coherent sum of the synthetic aperture rectangular sub-images formed for each element group. For the formation of each sub-image, the central element (relative to the group) transmits and all the group elements receive, using (1) and the apodization defined in Section 3.2. The envelope is then obtained from the absolute value of this combined image, which is in analytic signal form.

4. Results

To increase the processing speed and reduce the necessary data, less active receive elements in each group may be employed, consecutive and symmetric relative to the central transmit element. For example, with 9 active elements, there are 4 consecutive active elements to the left and 4 consecutive active elements to the right of the central element. In the arc method, it was noticed that when using many active receive elements the plot of the values along the arc showed double peaks (Fig. 12). The double peaks disappear when the number of active receive elements is reduced (Fig. 13). Simulations confirmed this behaviour (Figs. 12 and 13). The Figs. 14 and 15 show the arcs over the 2D image. In the case with 17 active receive elements, two peaks can be seen in the image, visualized by the contour lines. In addition, the center of the arc is not over the highest crest. This is what causes the double peaks. Simulations were run considering an array with a pitch of 0.15 mm, equivalent to $\lambda_l/2$, where λ_l is the wavelength in water at f_c, and considering cylinder radius R_{cyl} from 15 to 1000 mm. The simulation results showed no double peaks, indicating that they are caused by insufficient spatial sampling of the array. The experiments utilized an array with a pitch of 0.6 mm or $2\lambda_l$, four times larger than the ideal value.

This reduction in the active receive elements is only utilized in the surface detection phase. For image formation, all the elements in the group are used as receive elements.

Also for the arc method, the main lobe width and side lobe level were plotted for each number of active receive elements (Fig. 16 and 17). Fig. 16 shows the effects of the double peaks that occur when 11 or more active receive elements are utilized. Fig. 17 shows that the chosen threshold of 6 dB below the peak level only works with 7 or more active receive elements. Considering these two figures, the number of nine receive elements was chosen as the preferred value for the arc method, in these experiments. In other experimental configurations, for example

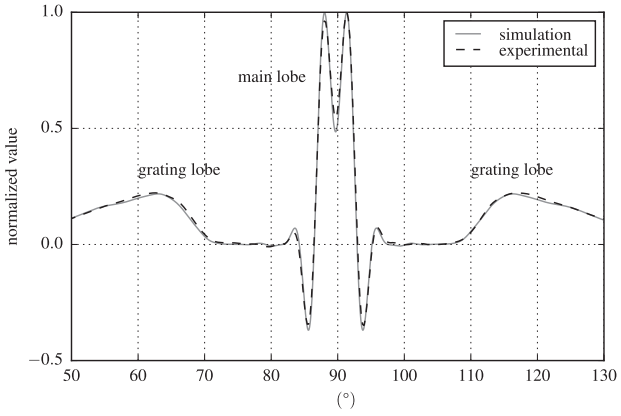

Fig. 12. Normalized values along the arc, in the arc method, for the central element group, $d = 20$ mm and 17 active receive elements.

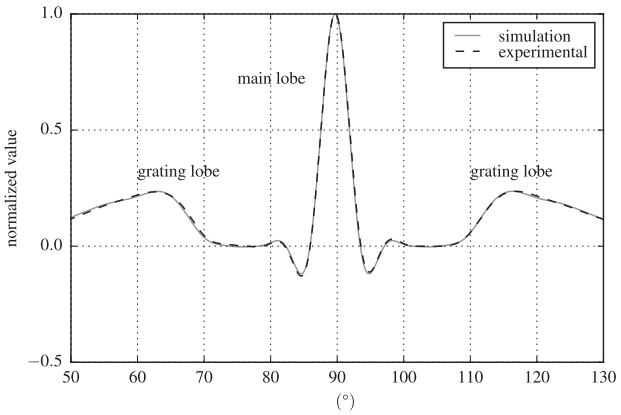

Fig. 13. Normalized values along the arc, in the arc method, for the central element group, $d = 20$ mm and 9 active receive elements.

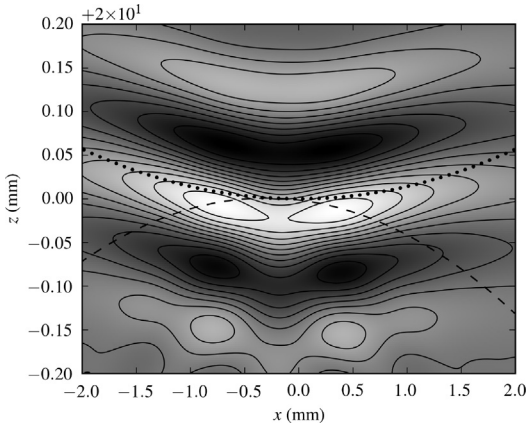

Fig. 14. The dashed line represents the arc defined in the arc method, over the simulated image, for the central element group, $d = 20$ mm and 17 active receive elements. The cylinder is represented by the dotted line.

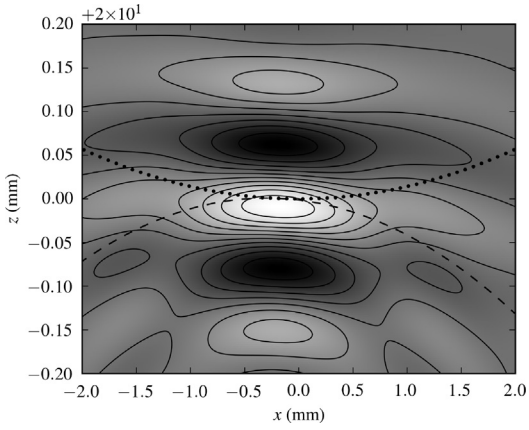

Fig. 15. The dashed line represents the arc defined in the arc method, over the simulated image, for the central element group, $d = 20$ mm and 9 active receive elements. The cylinder is represented by the dotted line.

with a different transducer, the curves may result different.

The arc method was able to use 7 or more active receive elements in simulations that were run considering cylinder radius R_{cyl} from 15 to 1000 mm.

Fig. 18 shows the error ε_{ref} for the arc method and nine active receive elements per group. The angle θ_p is defined in Fig. 1. The experiment is symmetric but the curves are not symmetric around $\theta_p = 0$, and the errors vary significantly for the different values of the distance

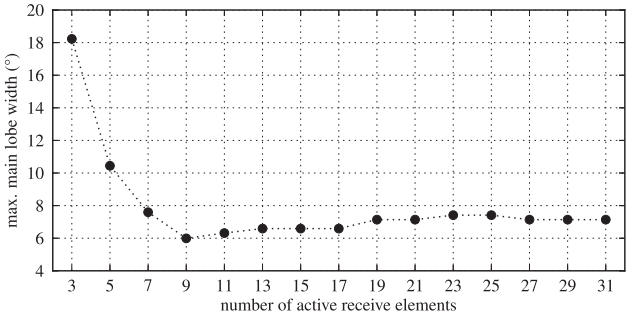

Fig. 16. Maximum main lobe width at −6 dB, in the arc method, considering all element groups and all the utilized values of the distance d, for each number of active receive elements.

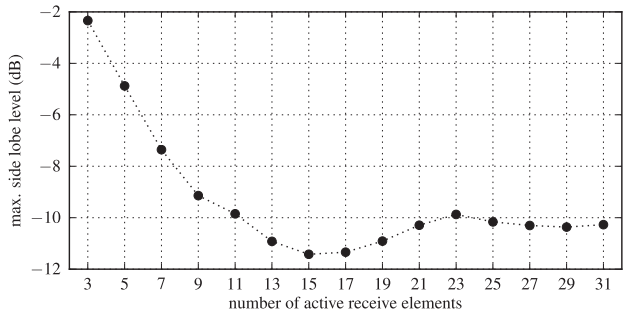

Fig. 17. Maximum side lobe level, relative to the main lobe level, in the arc method, considering all element groups and all the utilized values of the distance d, for each number of active receive elements.

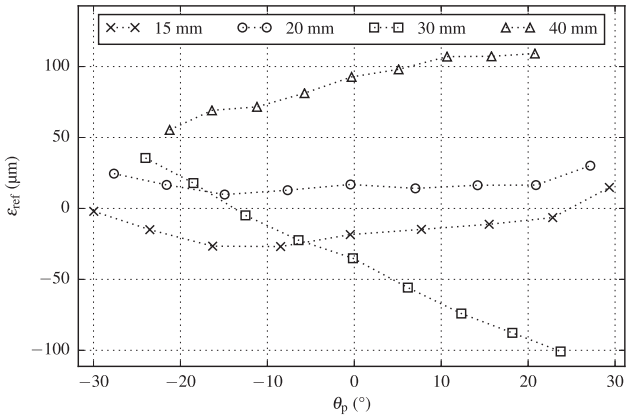

Fig. 18. Arc method: Errors between the detected point positions and the uncalibrated reference circle, for different values of the distance d.

d. For these reasons, the reference circles for each distance d were calibrated, to account for positioning errors. First the coordinate x_c of the center of the reference circle was set to $\bar{x}_c$, the coordinate of the fitted circle, due to the symmetry of the cylindrical block. Then the distance between the block and the array was measured by pulse-echo, using the two central array elements, one transmitting and the other receiving. The measured distance was used to adjust the coordinate z_c of the center of the reference circle. This distance measurement is influenced by errors in the propagation speed c_1 and in the reference signal s_{ref}, errors that are mostly compensated for when using the central element group, which is near the area where the measurement was made. But for other groups the effect of the errors may be stronger. As a consequence, with this calibration, the obtained experimental errors in the surface detection are only meaningful as a tool for comparison between the surface detection methods. This calibration is only needed in the error analysis.

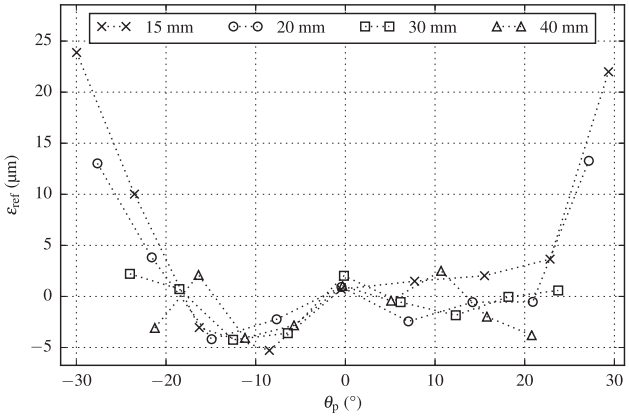

Fig. 19. Arc method: Errors between the detected point positions and the calibrated reference circle, for different values of the distance d.

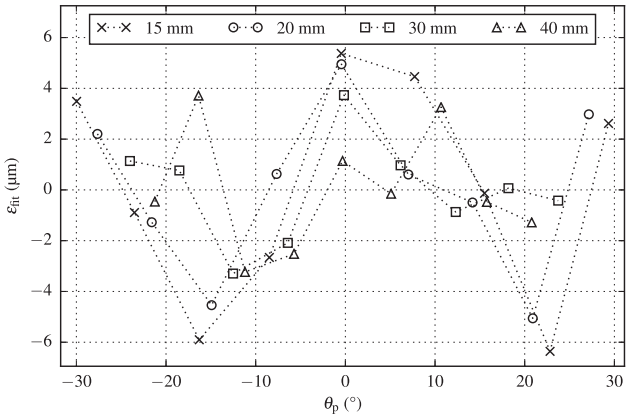

Fig. 20. Arc method: Errors between the detected point positions and the fitted circle, for different values of the distance d.

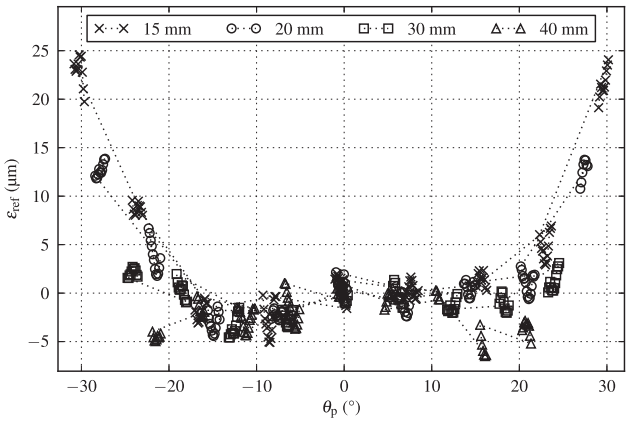

Fig. 21. Tangent curve method: Errors between the detected point positions and the calibrated reference circle, for different values of the distance d.

Figs. 19–24 show the surface detection errors for the arc, tangent curve and pitch-catch methods, with calibrated reference circle and nine active receive elements in each group. The figures for the tangent curve and pitch-catch methods are more cluttered, because the methods produce more points than the arc method, but it can be seen that the general behaviour is very similar to the arc method, with maximum error less than 35 µm, for all methods. And the error is larger for greater absolute values of θ_p. The errors between the detected point positions and the fitted circle are smaller, as expected.

The maximum RMS error between the detected points and the

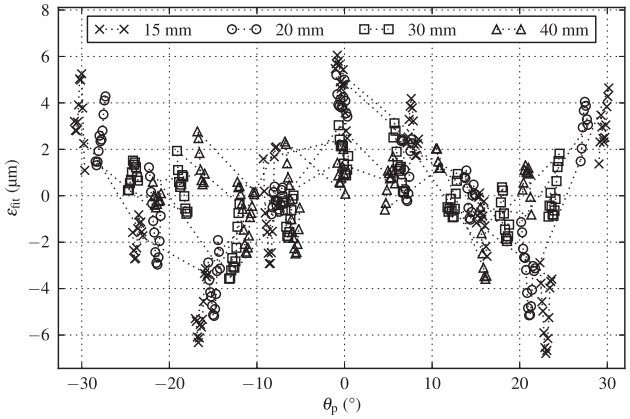

Fig. 22. Tangent curve method: Errors between the detected point positions and the fitted circle, for different values of the distance d.

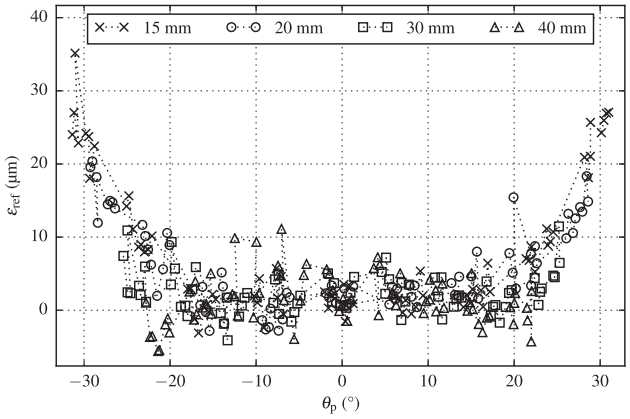

Fig. 23. Pitch-catch method: Errors between the detected point positions and the calibrated reference circle, for different values of the distance d.

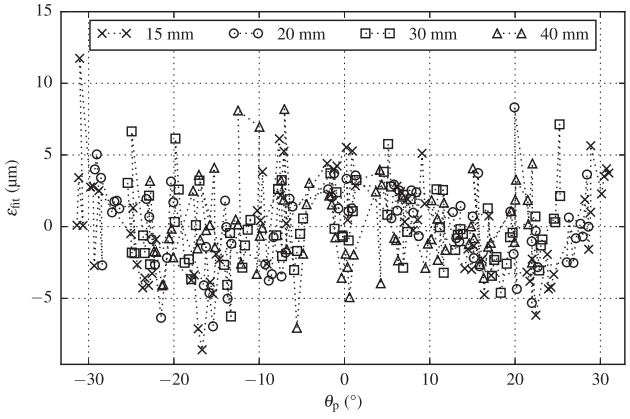

Fig. 24. Pitch-catch method: Errors between the detected point positions and the fitted circle, for different values of the distance d.

calibrated reference circle, for the arc, tangent curve and pitch-cath methods, were compared in Fig. 25, for different numbers of active receive elements. In the figure, the RMS error was calculated for each distance d, and the maximum value was plotted. With 23 or more active receive elements, the error for the tangent curve and pitch-catch methods increase significantly. These two methods did not handle well a high number of active receive elements in the experiments, and the errors were worsened by distortions in the shape of some signals that cause the peak value to be detected at a secondary lobe in the result of the cross-correlation. This distortion is caused by the directivity of the

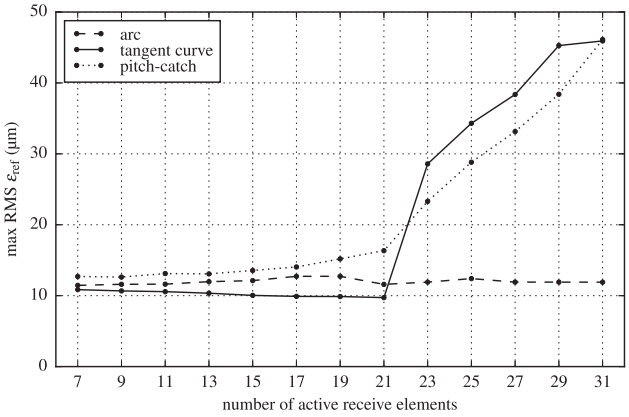

Fig. 25. Maximum RMS error between the detected point positions and the calibrated reference circle, considering all the utilized values of the distance d, for each number of active receive elements.

individual array elements. The leftmost and the rightmost element groups have the highest absolute values of θ_p, therefore higher errors were expected in those groups, also because of the directivity of the elements. The farther the receive element is from the central transmit element, the worse can become the problem of element directivity. This is why a high number of active receive elements can produce larger errors. To illustrate the problem, in Fig. 1, the rightmost element in the active group sees the point P farther from the z-direction, compared with the transmit element.

The tangent curve method produced smaller errors for groups with 7–21 active receive elements and the arc method, for groups with 23–31 active receive elements.

The pitch-catch was the only method that produced NaN (not a number) values for groups with 11 or more active receive elements. The NaN values were the result of square root of negative numbers. This shows a sensitivity to the noise present in the ultrasound signals. Filtering of outliers would solve this problem, but it has not been done in this work because the idea was to check how the methods would handle the noise.

The tangent curve method was also sensitive to noise in the signals. For 3 and 5 active receive elements, in some cases θ_{min} resulted greater than θ_{max} (the angles are defined in Fig. 5).

The combined image may be seen in Fig. 26, for $d = 20$ mm and using the interface detected by the arc method with nine active receive elements in each group. The echoes are correctly positioned and the resolution is approximately the same for all holes. The noise above the

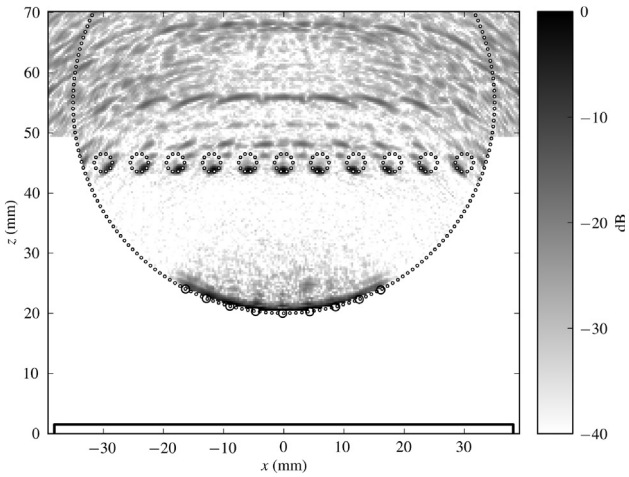

Fig. 26. Combined image for grid spacing $\lambda_2/4$, transmitting with only one element in each group.

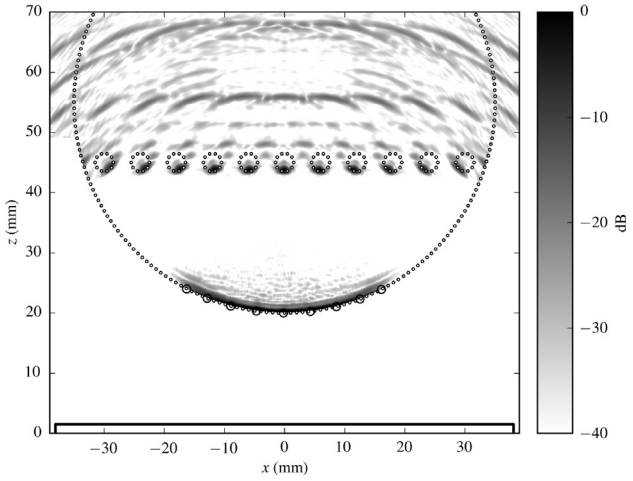

Fig. 27. Combined STA image for grid spacing $\lambda_2/16$, transmitting with all the elements in each group.

holes are reverberation due to multiple reflections in addition to echoes due to transverse waves.

In Fig. 27 an image formed by combination of Synthetic Transmit Aperture (STA) [17] images is shown. In STA all the elements in the group transmit, one by one, and all the group elements receive. The purpose of this image is to show the cost of using only one transmit element in each group. In the region between the holes and the part of the interface nearest to the transducer, the peak background noise level is 11 dB higher when using only one transmit element in each group. On the other hand, there is no significant difference in the resolution.

In Figs. 26 and 27 the dotted lines indicate the uncalibrated reference position of the aluminum block, the circles at the bottom of the interface indicate the points detected by the arc method, and the range of array elements is shown at the bottom of the image.

The acquisition equipment utilized in the experiments does not allow fast acquisition for synthetic aperture processing, consequently it was not possible to obtain a high enough transfer rate over the USB 2.0 bus, and for this reason the processing was done offline. The acquisition time was then estimated considering a pulse repetition frequency (PRF) of 5 kHz, and a transfer rate of 35 MB/s, which is a realistic value for "High-speed" USB 2.0 connections [18]. With an acquisition time equal to 85 µs at $f_s = 40$ MHz, and using 16-bit samples, the data size per image is 9 (acquisitions) × 2 (bytes/sample) × 3400 (samples) × 32 (receive channels) = 1.958 MB. With these parameters, the resulting total acquisition time is 9 (acquisitions) × (1/PRF) + 1.958 (data)/ 35 (transfer rate) = 57.7 ms. It is assumed that the acquisition sequence is automated, and only one data transfer is executed for each image.

The execution times shown in Table 1, for calculations in single precision, were obtained by the average of 20 executions. In the interface detection step 9 active receive elements were used in each group. The differences between the results in double and in single precision were measured, for each value of the distance d. For the arc method, the maximum distance between the corresponding points detected using the two floating point precisions was 0.0063 µm. For the tangent curve method, the value obtained was 0.72 µm, and for the pitch-catch method, 1.0 µm. In the image formation step, the maximum difference was at a level of −82 dB. The small differences indicate that single precision is adequate for the calculations. The performance tests were executed in single precision, but the comparison of surface detection methods was done in double precision.

Table 1
Execution times in ms.

Operation	Arc	Tangent curve	Pitch-catch
Acquisition (estimated)	57.7	57.7	57.7
Interface detection	5.30	4.72	4.72
Interface detection disregarding signal preparation	0.484	9.38×10^{-3}	1.03×10^{-3}
Circle fitting	1.46×10^{-4}	5.24×10^{-4}	3.89×10^{-4}
Image formation	33.6	33.6	33.6

Considering that the acquisition and the processing are executed consecutively, using the arc method, the calculated frame rate is 10.3 Hz. The total latency due to the acquisition, interface detection, circle fitting and the image formation, also for the arc method, resulted in 96.6 ms. Executing the next acquisition and data transfer while the previous data is being processed could increase the frame rate [19].

For the performance measurements a grid spacing of $\lambda_2/4$ was utilized in the image formation, resulting in an image with 244 columns and 160 rows, or 39,040 points. But since the points below the interface were not processed, the effective number of points was 30,511.

In the surface detection phase, the signal preparation occupies the greatest part of the processing time (Table 1). In the arc method, 90.9% of the time is spent on the preparation; in the tangent curve method, 99.8%, and in the pitch-catch method, 99.98%. Not considering the preparation, the arc method processing was approximately 50 times slower than the tangent curve method, which was 9 times slower than the pitch-catch method. All the tested surface detection methods were executed in less than 1 ms.

To simulate the effects of errors in the interface detection, offset values were added to the center and radius of the circle detected by the arc method, and the combined image was formed using this altered interface. Fig. 28a shows the image formed using the original interface. In Fig. 28b, $\bar{z}_c$ was reduced by 2.1 mm and $\bar{R}_{cyl}$ was reduced by 1.95 mm, resulting in a maximum absolute error of 0.15 mm or $\lambda_1/2$ in the region in which θ_p is between -30° and 30°, the region of detected points. This simulation of errors is an extreme case, with large differences between the assumed and the reference interfaces outside the region of detected points, but it shows that errors in the interface detection of tenths of a millimeter may cause significant distortions in the image.

5. Conclusions

The tangent curve method produced smaller errors when using less active receive elements per group. The arc method produced smaller errors when using more active receive elements per group, showing the robustness of imaging-based approaches, but the fact that it only detects one point per element group is a disadvantage. The pitch-catch method was the fastest of the three.

In the arc method, as the number of active receive elements is increased, so is the processing time, while producing the same amount of detected points. Therefore the advantage in accuracy for high number of active receive elements, compared with the other methods, may not be useful in practice. One possibility is the utilization of the method in noisy environments where the noise cannot be eliminated by averaging, or when there is enough parallel processing power available. Another disadvantage of the arc method is the need to assess its efficacy and accuracy experimentally for each configuration of transducer, object

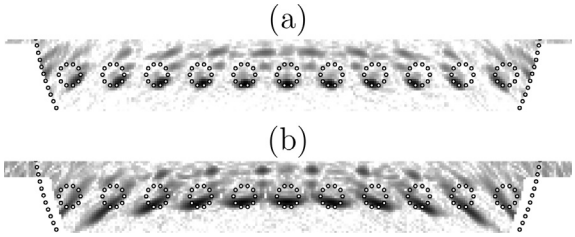

Fig. 28. Effects of simulated errors in the interface detection: (a) with no errors and (b) with errors limited by $\pm\,\lambda_1/2$. The dynamic range is 40 dB.

shape and relative position, because the method is not generic.

One important result is that using more active receive elements per group may not be good for accuracy (see Fig. 25). The processing is also heavier. The tangent curve and pitch-catch methods clearly have their accuracy decreased for high number of active receive elements, even though their accuracy may be enough for conventional applications. For a low number of active receive elements, the three surface detection methods were almost equivalent in accuracy. In this condition the pitch-catch method is the best choice due to its speed.

The accuracy comparison between the surface detection methods was based on a limited set of experiments, therefore it can not be generalized. However, the fact that none of the analyzed methods was a clear winner is a motivation for the development of new surface detection methods that combine genericity, robustness, performance and high accuracy.

If the signal preparation is considered, the arc method is not much slower then the other two methods. This shows that the performance of the analyzed surface detection methods is not a limitation for interactive two-medium ultrasound imaging. The signal preparation could be executed on an FPGA in the acquisition device, but in this case the connection between the acquisition device and the PC should be faster, due to the greater amount of data.

In the surface detection phase, the choice of the number of active receive elements must first consider the minimum value. A number that is too low may cause problems with the tangent curve method, due to its sensitivity to noise in the signals. In the case of the arc method, the low number may make impossible the use of a given threshold. Then the choice is between lower numbers, with better performance and smaller errors, or higher numbers, which lead to more interface points in the tangent curve and pitch-catch methods. A larger number of interface points may reduce the error in the curve fitting step due to averaging, but Figs. 21 and 23 show that the errors may not have zero mean, which can cause a deviation in the fitted curve. This analysis must be also done experimentally for each configuration of transducer, object shape and relative position, especially due to the nontrivial effect of the noise in the experimental signals.

The combination of images was effective, producing no visible artifacts. The estimated frame rate for acquisition, the analyzed surface detection methods and image formation, running on a general-purpose CPU, allows interactive testing, even using the slowest method (arc method). The processing on the CPU can reduce the complexity of the acquisition system.

The execution times for the surface detection step are much shorter than the acquisition and the image formation times, therefore it is more useful to optimize the acquisition and the image formation processing. The acquisition time may be reduced with the utilization of a faster bus between the acquisition device and the PC, for example USB 3.0. The image formation can be accelerated, for example, by a more optimized software, but if the user needs higher image resolutions the utilization of General-Purpose GPUs (GPGPU) may be considered, due to their higher memory bandwidth and parallel processing capabilities.

Acknowledgment

This work was supported by CAPES, FAPESP and Petrobras/ANP. During the final revision this work was supported by Shell.

References

[1] O. Casula, C. Poidevin, G. Cattiaux, P. Dumas, Control of complex components with smart flexible phased arrays, Ultrasonics 44 (Supplement) (2006) e647–e651, https://doi.org/10.1016/j.ultras.2006.05.122 proceedings of Ultrasonics International (UI'05) and World Congress on Ultrasonics (WCU).

[2] O. Keitmann-Curdes, P. Knoll, H. Meier, H. Ermert, Contour tracking of specularly reflecting surfaces, Ultrasonics 44 (Supplement) (2006) e1089–e1092, https://doi.org/10.1016/j.ultras.2006.05.105 proceedings of Ultrasonics International (UI'05) and World Congress on Ultrasonics (WCU).

[3] M.Y. Matuda, F. Buiochi, J.C. Adamowski, Imaging through a convex interface with unknown position and shape using an ultrasonic linear array, AIP Conf. Proc. 1433 (1) (2012) 177–180, https://doi.org/10.1063/1.3703165.

[4] B. Barshan, Ultrasonic surface profile determination by spatial voting, Electron. Lett. 35 (25) (1999) 2232–2234, https://doi.org/10.1049/el:19991477.

[5] S. Kidera, T. Sakamoto, T. Sato, A robust and fast imaging algorithm without derivative operations for UWB pulse radars, First European Conference on Antennas and Propagation, 2006. EuCAP 2006, 2006, pp. 1–6, , https://doi.org/10.1109/EUCAP.2006.4584899.

[6] S. Robert, O. Casula, O. Roy, G. Neau, Real-time inspection of complex composite structures with a self-adaptive ultrasonic technique, 18th World Conference on Nondestructive Testing, 2012, pp. 1–9.

[7] J. Camacho, J. Cruza, J. Brizuela, C. Fritsch, Automatic dynamic depth focusing for NDT, IEEE Trans. Ferroelectr. Freq. Control 61 (4) (2014) 673–684, https://doi.org/10.1109/TUFFC.2014.2955.

[8] M. Sutcliffe, M. Weston, P. Charlton, K. Donne, B. Wright, I. Cooper, Full matrix capture with time-efficient auto-focusing of unknown geometry through dual-layered media, Insight - Non-Destruct. Test. Cond. Monitor. 55 (6) (2013) 297–301, https://doi.org/10.1784/insi.2012.55.6.297 307.

[9] J.-F. Aubry, D. Cassereau, M. Tanter, T. Pellegrini, M. Fink, Skull surface detection algorithm to optimize time reversal focusing through a human skull, Ultrasonics Symposium, 2002. Proceedings. 2002 IEEE, vol. 2, 2002, pp. 1451–1454, , https://doi.org/10.1109/ULTSYM.2002.1192570.

[10] E.W. Weisstein, Ellipse. From MathWorld – A Wolfram Web Resource, <http://mathworld.wolfram.com/Ellipse.html>, Oct. 2018.

[11] W. Marczak, Water as a standard in the measurements of speed of sound in liquids, J. Acoust. Soc. Am. 102 (5) (1997) 2776–2779, https://doi.org/10.1121/1.420332.

[12] S.M. Gehlbach, R.E. Alvarez, Digital ultrasound imaging techniques using vector sampling and raster line reconstruction, Ultrason. Imag. 3 (1) (1981) 83–107, https://doi.org/10.1016/0161-7346(81)90083-3.

[13] V. Pratt, Direct least-squares fitting of algebraic surfaces, SIGGRAPH Comput. Graph. 21 (1987) 145–152, https://doi.org/10.1145/37402.37420.

[14] N. Chernov, C. Lesort, Least squares fitting of circles, J. Math. Imag. Vision 23 (3) (2005) 239–252.

[15] M. Weston, P. Mudge, C. Davis, A. Peyton, Time efficient auto-focussing algorithms for ultrasonic inspection of dual-layered media using Full Matrix Capture, NDT & E Int. 47 (2012) 43–50, https://doi.org/10.1016/j.ndteint.2011.10.006.

[16] M. Parrilla, J. Brizuela, J. Camacho, A. Ibaez, P. Nevado, C. Fritsch, Dynamic focusing through arbitrary geometry interfaces, Ultrasonics Symposium, 2008. IUS 2008, IEEE, 2008, pp. 1195–1198, , https://doi.org/10.1109/ULTSYM.2008.0288.

[17] K.L. Gammelmark, J.A. Jensen, Multielement synthetic transmit aperture imaging using temporal encoding, IEEE Trans. Med. Imag. 22 (4) (2003) 552–563, https://doi.org/10.1109/TMI.2003.809088.

[18] E. Boni, A. Cellai, A. Ramalli, P. Tortoli, A high performance board for acquisition of 64-channel ultrasound RF data, 2012 IEEE International Ultrasonics Symposium (IUS), 2012, pp. 2067–2070, , https://doi.org/10.1109/ULTSYM.2012.0517.

[19] M. Sutcliffe, M. Weston, B. Dutton, P. Charlton, K. Donne, Real-time full matrix capture for ultrasonic non-destructive testing with acceleration of post-processing through graphic hardware, NDT & E Int. 51 (2012) 16–23, https://doi.org/10.1016/j.ndteint.2012.06.005.